

# Gold Nanostars Coated with Mesoporous Silica Are Effective and Nontoxic Photothermal Agents Capable of Gate Keeping and Laser-Induced Drug Release

Andy Hernández Montoto,<sup>†</sup> Roberto Montes,<sup>†</sup> Akbar Samadi,<sup>†,‡,§,||</sup> Mónica Gorbe,<sup>†,||</sup> José Manuel Terrés,<sup>†</sup> Roberto Cao-Milán,<sup>#,||</sup> Elena Aznar,<sup>†,‡,§,||</sup> Javier Ibañez,<sup>†</sup> Rafael Masot,<sup>†</sup> María Dolores Marcos,<sup>†,‡,§,||</sup> Mar Orzáez,<sup>||</sup> Félix Sancenón,<sup>†,‡,§,||</sup> Lene B. Oddershede,<sup>\*,†,||</sup> and Ramón Martínez-Mañez<sup>\*,†,‡,§,||</sup>

<sup>†</sup>Instituto Interuniversitario de Investigación de Reconocimiento Molecular y Desarrollo Tecnológico (IDM), Universitat Politècnica de València, Universitat de València, Camino de Vera s/n, 46022 València, Spain

<sup>‡</sup>CIBER de Bioingeniería, Biomateriales y Nanomedicina (CIBER-BBN), Spain

<sup>§</sup>Departamento de Química, Universitat Politècnica de València, Camino de Vera s/n, 46022 València, Spain

<sup>||</sup>Unidad Mixta UPV-CIPF de Investigación en Mecanismos de Enfermedades y Nanomedicina, Valencia, Universitat Politècnica de València, Centro de Investigación Príncipe Felipe, 46012 València, Spain

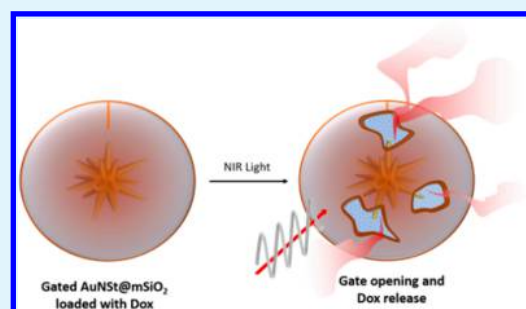
<sup>†</sup>Niels Bohr Institute, University of Copenhagen, 2100 Copenhagen, Denmark

<sup>#</sup>Facultad de Química, Universidad de La Habana, 10400 La Habana, Cuba

## Supporting Information

**ABSTRACT:** Herein, a novel drug photorelease system based on gold nanostars (AuNSts), coated with a mesoporous silica shell and capped with paraffin as thermosensitive molecular gate, is reported. Direct measurements of the surface temperature of a single gold nanostar irradiated using a tightly focused laser beam are performed via a heat-sensitive biological matrix. The surface temperature of a AuNSt increases by hundreds of degrees (°C) even at low laser powers. AuNSts coated with a mesoporous silica shell using a surfactant-templated synthesis are used as chemotherapeutic nanocarriers. Synthetic parameters are optimized to avoid AuNSt reshaping, and thus to obtain nanoparticles with suitable and stable plasmonic properties for near-infrared (NIR) laser-triggered cargo delivery. The mesoporous silica-coated nanostars are loaded with doxorubicin (Dox) and coated with octadecyltrimethoxysilane and the paraffin heneicosane. The paraffin molecules formed a hydrophobic layer that blocks the pores, impeding the release of the cargo. This hybrid nanosystem exhibits a well-defined photodelivery profile using NIR radiation, even at low power density, whereas the nonirradiated sample shows a negligible payload release. Dox-loaded nanoparticles displayed no cytotoxicity toward HeLa cells, until they are irradiated with 808 nm laser, provoking paraffin melting and drug release. Hence, these novel, functional, and biocompatible nanoparticles display adequate plasmonic properties for NIR-triggered drug photorelease applications.

**KEYWORDS:** gold nanostars, mesoporous silica shell, thermosensitive molecular gates, optical heating, drug photorelease



## INTRODUCTION

Drug release systems remotely controlled by near-infrared (NIR) light irradiation have received increasing attention in cancer therapy because cargo release can be defined spatially and temporally by choosing the time and area of irradiation.<sup>1,2</sup> Moreover, the use of NIR radiation (700–1100 nm) is especially appealing for biological/medical applications due to its high penetration power and minimal healthy tissue damage.<sup>3</sup> Currently, studies have been focused on finding different ways to create complex systems based on nanoparticles which can simultaneously store drugs efficiently and activate a mechanism for its delivery using NIR light irradiation.<sup>4–6</sup>

Because of their pronounced localized surface plasmon resonance (LSPR), anisotropic gold nanoparticles efficiently absorb NIR light transforming it to thermal energy.<sup>7–9</sup> Among anisotropic gold nanoparticles, gold nanostars (AuNSts), with multiple sharp branches, have superior light-to-heat conversion efficiency<sup>10–12</sup> due to the strong amplification of electromagnetic field at their sharp tips, which act as multiple hot spots.<sup>13,14</sup> For an evaluation and comparison of the heating efficiency of individual nanoparticles and thereby their

Received: May 21, 2018

Accepted: July 24, 2018

Published: July 24, 2018

potential application for cancer therapy (such as hyperthermia and photothermal-triggered drug delivery), it is important to assess the exact temperature profile around a single irradiated nanoparticle. For direct measurement of the temperature profile of an irradiated nanoparticle, one can use a biological matrix with a well-defined phase transition temperature as sensor as demonstrated for various types of nanoparticles,<sup>15–17</sup> however, not yet for AuNSts.

On the other hand, mesoporous silica (MS) materials are especially appealing as drug nanocarriers because they possess unique properties, such as high loading capacity, chemical stability, biocompatibility, and low cost. These materials can be obtained in different forms (micro- or nanoparticles), and have tailor-made pores (2–10 nm in diameter) and large volumes and surface areas (up to 1200 m<sup>2</sup> g<sup>-1</sup>). Moreover, the external surface of mesoporous materials can be modified with supramolecular or (bio)chemical ensembles than act as “molecular gates”. These gated materials are able to control the diffusion of loaded drug inside the mesoporous channels upon the application of an external stimulus.<sup>1</sup>

There are few photodelivery systems reported in the literature that combine plasmonic gold nanoparticles and gated mesoporous materials.<sup>1</sup> These reported systems are based on gold nanorods<sup>18–23</sup> or nanocages<sup>24</sup> coated with a MS shell and capped with thermosensible gatekeepers, such as smart polymers,<sup>19,24</sup> phase-changing materials,<sup>18</sup> oligonucleotides,<sup>20–22</sup> and supramolecular switches.<sup>23</sup> However, AuNSts coated with a gated mesoporous silica shell have not yet been employed for NIR-laser-triggered photorelease applications in spite of their superior plasmonic properties,<sup>10–12</sup> and their use in intracellular imaging<sup>25,26</sup> and photothermal therapy applications.<sup>27,28</sup>

We report herein an optimization of the synthesis of AuNSts coated with a mesoporous silica shell (AuNSt@mSiO<sub>2</sub>). Also, we quantify the heating and drug release capabilities of the MS-coated AuNSts relevant for controlled release applications using NIR irradiation. To this end, AuNSt@mSiO<sub>2</sub> nanoparticles were loaded with a cytotoxic drug (Dox) and capped with the paraffin heneicosane (AuNSt@mSiO<sub>2</sub>@Dox@paraffin). We found that unirradiated AuNSt@mSiO<sub>2</sub>@Dox@paraffin nanoparticles remained capped with a negligible leak of cargo. Irradiation with 808 nm light produces a temperature enhancement in the surroundings of the AuNSts and melting of the gating paraffin, and induces the cargo release. Dox-loaded nanoparticles show no cytotoxicity toward HeLa cells until they are irradiated with 808 nm laser, corroborating the gating efficiency of paraffin and the activation mechanism of drug release due to the photothermal conversion by AuNSts. Also, using a biological matrix we quantified the temperature profile around a NIR-irradiated single bare or polymer-coated (PVP-coated; PVP, polyvinylpyrrolidone) AuNSt. The heating associated with NIR irradiation of AuNSts is dependent on laser power and on whether or not the AuNSt is coated with the polymer. Both with and without coating, temperatures up to 100 °C, more than sufficient for cancer treatment, could be reached at relatively low laser powers (less than 50 mW).

## EXPERIMENTAL SECTION

**Chemicals.** Tetrachloroauric acid aqueous solution 30%, sodium citrate trihydrate, polyvinylpyrrolidone (PVP,  $M_w = 10\,000$ ), *N,N*-dimethylformamide (DMF), hexadecyltrimethylammonium bromide (CTAB), tetraethoxysilane (TEOS), ammonia aqueous solution 32%, ammonium nitrate, octadecyltrimethoxysilane, and heneicosane were

purchased from Aldrich. Doxorubicin hydrochloride was purchased from Carbosynth Limited. Solvents of analytical grade were purchased from Scharlau. HeLa cells were purchased from the German Resource Center for Biological Materials. Fetal bovine serum (FBS), Dulbecco's modified Eagle's medium (DMEM), Dulbecco's phosphate buffer saline (PBS), trypsin, Hoechst 33342, and cell proliferation reagent WST-1 were purchased from Sigma-Aldrich.

**Instrumentation.** Transmission electron microscopy (TEM) images were acquired using a JEOL JEM-1010 microscope operating at 100 kV. Dark-field scanning transmission electron microscopy (HAADF-STEM) images, energy-dispersive X-ray spectra (EDXS), and EDXS element mapping were collected on a JEOL JEM-2100F microscope operating at 200 kV. Field-emission scanning electron microscopy (FE-SEM) images were taken on a ZEISS ULTRA55 microscope. Optical extinction spectra were acquired using a JASCO V-650 UV/vis spectrophotometer. Fluorescence spectra were recorded on a JASCO FP-8300 spectrofluorometer (Hitachi High Technologies). Fourier transform infrared (FT-IR) spectra were obtained using a Bruker TENSOR27 spectrometer. X-ray measurements were carried out on a Bruker AXS D8 Advance diffractometer using Cu K $\alpha$  radiation. Thermogravimetric analyses were performed on a TGA/SDTA 851e Mettler Toledo apparatus, using an oxidant atmosphere (air, 80 mL min<sup>-1</sup>) with a heating program which consisted of a heating step from 298 to 373 K at heating rate of 10 K min<sup>-1</sup>, and then an isothermal heating step at 373 K for 30 min, a third heating step from 373 to 1273 K at heating rate of 10 K min<sup>-1</sup>, and finally an isothermal heating step at 1273 K for 30 min. N<sub>2</sub> adsorption–desorption isotherms were obtained on a Micromeritics ASAP2010 automated sorption analyzer. The samples were degassed at 120 °C under vacuum overnight. The specific surface areas were determined from the adsorption data in the low-pressure range using the Brunauer–Emmett–Teller (BET) method. Pore size was calculated by following the Barrett–Joyner–Halenda (BJH) model.  $\zeta$  potential and hydrodynamic diameter measurements were performed by dynamic light scattering using a Malvern Zetasizer Nano ZS instrument.

**Synthesis of 15 and 40 nm Gold Nanosphere Seeds.** Citrate-coated gold nanoparticles with diameters of 15 and 40 nm were obtained by Turkevich–Frens method<sup>29–31</sup> and Bastús protocol,<sup>32</sup> respectively. Both nanoparticle samples were coated with PVP according to the procedure reported by Graf et al.<sup>33</sup> The concentration of Au in nanoparticle suspensions was obtained from their optical extinction spectra ( $\epsilon = 2400\text{ L mol}^{-1}\text{ cm}^{-1}$  at 400 nm).<sup>34,35</sup>

**Synthesis of Bare Gold Nanostars (AuNSts).** AuNSts were synthesized by seeded growth method employing a PVP solution in DMF with minor modification.<sup>36–38</sup> At 25 °C, an aqueous solution of HAuCl<sub>4</sub> (750  $\mu\text{L}$ ; 166 mM) was mixed with a PVP solution in DMF (150 mL; 10 mM). After 5 min, a preformed seed dispersion (100  $\mu\text{L}$ ; 15 nm gold nanospheres coated with PVP in ethanol,  $c(\text{Au}) = 6.5\text{ mM}$ ) was added and allowed to react for 24 h without stirring. Gold nanoparticles were recovered by centrifugation (20 min; 9500 rpm) and washed five times with water by centrifugation and redispersion. The nanoparticle concentration in the AuNSt sample was calculated using the number of Au atoms per particle that can be estimated assuming that AuNSts have a quasispherical morphology to determine nanoparticle volume from TEM images. The detailed calculation procedure of nanoparticle concentration in AuNSts is included in the Supporting Information.

**Synthesis of PVP-Coated AuNSts (AuNSt@PVP).** AuNSts were synthesized by seeded growth method using a PVP solution in DMF with minor modification.<sup>36–38</sup> At 25 °C, an aqueous solution of HAuCl<sub>4</sub> (750  $\mu\text{L}$ ; 166 mM) was mixed with a PVP solution in DMF (150 mL; 10 mM). After 5 min, a preformed seed dispersion (100  $\mu\text{L}$ ; 40 nm Au nanospheres coated with PVP in ethanol,  $c(\text{Au}) = 8.5\text{ mM}$ ) was added and allowed to react for 24 h without stirring. Au nanoparticles were recovered by centrifugation (20 min; 9500 rpm) and washed one time with water by centrifugation and redispersion.

**Synthesis of Mesoporous Silica-Shell-Coated AuNSts (AuNSt@mSiO<sub>2</sub>).** At 25 °C, a CTAB aqueous solution (50 mL;

6.6 mM) was mixed with ethanol (20 mL) in a round-bottom flask (250 mL) under magnetic stirring (400 rpm). Ar gas was bubbled into solution for 1 h, and then inert atmosphere was kept until the reaction was completed. Once the solution was free of Ar bubbles, an ammonia aqueous solution (50  $\mu\text{L}$ ; 32%) was added. Subsequently, a bare AuNSt dispersion (3 mL;  $c(\text{Au}) = 5 \text{ mM}$ ) was added to the reaction mixture. After 5 min, a predetermined volume of TEOS (30–40  $\mu\text{L}$ ) was added dropwise. The TEOS amount in the reaction mixture was varied to obtain the desired nanoparticle size. After 24 h the particles were recovered (10 min, 9500 rpm) and washed twice in ethanol. Finally, the CTAB template was removed by extraction process dispersing nanoparticles in a  $\text{NH}_4\text{NO}_3$  solution in ethanol (50 mL; 10 mg  $\text{mL}^{-1}$ ). The mixture was stirred for 8 h, and particles were recovered by centrifugation. This extraction procedure was repeated three times to achieve the removal of a higher amount of CTAB from mesoporous channels.

**Cargo Loading.** The loading of Dox within the mesopores of AuNSt@mSiO<sub>2</sub> nanoparticles and its subsequent functionalization with octadecyl chains were performed following a procedure previously reported by our group with minor modification.<sup>39</sup> Briefly, AuNSt@mSiO<sub>2</sub> nanoparticles (2 mg) were dispersed in ethanol (2 mL). Subsequently, doxorubicin hydrochloride (1 mg) and octadecyltrimethoxysilane (20  $\mu\text{L}$ ) were added. The mixture was stirred for 12 h at 25 °C. The nanoparticles were recovered by centrifugation and dried under vacuum. Then, Dox-loaded nanoparticles were dispersed in *n*-hexane (10 mL), and a heneicosane solution in *n*-hexane (1 mL; 20 mg  $\text{mL}^{-1}$ ) was added. The mixture was dispersed for short periods (1 min) during 30 min using an ultrasonic bath, and the nanoparticles were recovered by centrifugation and dried under vacuum. The overall fraction of organic materials was estimated by TGA measurements. The amount of loaded Dox was calculated by spectrophotometry, dispersing AuNSt@mSiO<sub>2</sub>@Dox@paraffin nanoparticles (1 mg) in water (1 mL). Then, the nanoparticle suspension was stirred at 60 °C for 48 h to extract and transfer Dox into water. Finally, after centrifugation of nanoparticles, the absorbance at 480 nm of the supernatant was used to determine the amount of Dox employing a predetermined calibration curve. The detailed calculation procedure of Dox content in nanoparticles is included in the [Supporting Information](#).

**Cargo Photorelease.** Before the cargo photorelease experiment was performed, AuNSt@mSiO<sub>2</sub>@Dox@paraffin nanoparticles were washed several times with water by centrifugation and redispersion. The NIR-laser-triggered drug release experiments were performed with a laser diode (808 nm)<sup>40</sup> that was set at 1 cm above the liquid surface. A well in the 96-well plate was filled with nanoparticle suspensions (250  $\mu\text{L}$ ; 100  $\mu\text{g mL}^{-1}$ ). This well and another containing a control sample were placed in an air chamber at 37 °C. Then, the nanoparticle suspension was irradiated at a predetermined power density (0.4 and 4  $\text{W cm}^{-2}$ ). At a predetermined interval upon NIR irradiation, the samples were centrifuged (3 min, 9500 rpm), and the released cargo from supernatant was calculated from the fluorescence emission spectra of Dox ( $\lambda_{\text{em}} = 555 \text{ nm}$ ;  $\lambda_{\text{exc}} = 488 \text{ nm}$ ). Temperature changes of control and irradiated samples were recorded employing a fiber-optic thermosensor.

**Cell Viability Assays.** HeLa cells were grown at 37 °C under humidified air containing CO<sub>2</sub> (5 vol %) in DMEM, which was supplemented with fetal bovine serum (10 vol % FBS, Gibco) and penicillin/streptomycin (1 vol %; 10 000 units of both per mL). After 24 h of incubation, cells were rinsed with PBS, and then detached with trypsin (0.2 vol %)/PBS. The HeLa cells were seeded in 96-well plates (density of  $5 \times 10^3$  cells per well) and grown in DMEM for 24 h. The cells were then treated with the nanoparticle suspensions in DMEM at different concentrations. Then, the designated cells were irradiated with an NIR laser (808 nm, 1–4  $\text{W cm}^{-2}$ , 10–15 min). After laser irradiation, the treated cells were incubated for another 24 or 48 h. After a predetermined incubation period, the cells were rinsed with PBS, and the cell viabilities were evaluated via the WST-1 assay. Typically, cell proliferation reagent WST-1 (7  $\mu\text{L}$ ) was added, and then, the cells were incubated for another 1 h at 37 °C. The

absorbance at 450 nm was measured employing a plate reader (PerkinElmer Wallac 1420 Victor2). Percentages of cell viabilities were calculated relative to the control cells (100% viability). Three replicates were done for each treatment group.

For NIR-light-triggered Dox delivery experiments using confocal laser scanning microscopy (CLSM), cells were seeded over glass coverslips in a 6-well plate with a density of  $5 \times 10^5$  cells per well and grown in DMEM for 24 h. Cells were incubated with AuNSt@mSiO<sub>2</sub>@Dox@paraffin nanoparticles at 10 and 50  $\mu\text{g mL}^{-1}$  for 2 h. Then, the designated cells were irradiated with 808 nm laser at 4  $\text{W cm}^{-2}$  for 10 min and were incubated for another 2 h. Cells were rinsed with PBS, and DMEM was freshly added. Finally, DNA marker Hoechst 33342 (2  $\mu\text{g mL}^{-1}$ ) was added, and cells were incubated for 5 min before CLSM analysis. CLSM images were recorded using a Leica TCS SP8 (Leica Microsystems CMS GmbH) confocal laser scanning microscope.

Cell internalization of nanoparticles was tested by TEM. TEM images were acquired using a microscope FEI Tecnai Spirit G2 operating at 80 kV with a digital camera (Soft Image System, Morada). HeLa cells were incubated with nanoparticle suspension in DMEM at 30  $\mu\text{g mL}^{-1}$  for 24 h. Then, cells were fixed with glutaraldehyde (3%) in sodium phosphate buffer (0.1 mol  $\text{L}^{-1}$ ), dehydrated in ethanol, and stained with uranyl acetate (1%) and osmium tetroxide (1%). Finally, the samples were embedded in epoxy resin (Araldite) and sectioned for analysis.

**Direct Measurements of the Temperature Profile of Irradiated Single AuNSts.** These measurements were done accordingly to the protocols first published by Bendix et al.<sup>15</sup> To mark the gel phase we used 1,2-dipentadecanoyl-*sn*-glycero-3-phosphocholine (DC<sub>15</sub>PC, Avanti Polar lipids) with 3,3'-dilinoleoyloxycarbocyanine perchlorate (0.75 mol % DiOC<sub>18:2</sub>) fluorophores which were excited by 488 nm and imaged in the spectral range 496–587 nm.<sup>16</sup> These lipids were suspended in chloroform, put on glass, and dried first under nitrogen flow and afterward in vacuum for 2 h. After this we hydrated the lipid layer in PBS buffer at 37 °C. The lipids were then extruded through 50 nm filters to form small unilamellar vesicles (SUVs). These SUVs were incubated with a hydrophilic glass surface for 3 h at 37 °C. This temperature is above the lipid's phase transition, thus keeping it in a disordered state. The glass surface was afterward washed thoroughly by Milli-Q water while still keeping the sample at 37 °C. Then, we added nanoparticles, suspended in Milli-Q water, to the sample. Most particles would adhere to the bilayer, and only those which were firmly stuck would be used for the experiments. During all experiments, the temperature was controlled by a circulating water bath with a precision of  $\sim 0.5$  °C.

The NIR laser employed for quantifying the temperature profile of irradiated AuNSts had a wavelength of 1064 nm (Physics Millennium, TEM00, Nd:YVO<sub>4</sub>) and was implemented in a Leica confocal laser scanning microscope (SP5/TCS). Details on the setup can be found in ref 41. A high-numerical-aperture (high-NA) objective (HC, PL, APO, 63.X, NA = 1.20 WATER) tightly focused the laser light. A 3D piezo stage (PI 731.20, Physik Instrumente) was used to position the sample with respect to the focus of the laser. We used the reflection mode of the confocal microscope (with a wavelength of 594 nm) to image the metallic nanoparticles.

The intensity at the focus is given by  $I = \frac{4P}{\pi d_{\text{spot}}^2}$ . To estimate  $I$ , we used the focused NIR laser to bleach an area of the lipid bilayer (in the gel state) and measured the spot-size,  $d_{\text{spot}}$  to be 1.95  $\mu\text{m}$ . Using the dual-objective method, we directly measured  $P$ .

## RESULTS AND DISCUSSION

Although the use of AuNSts coated with a gated mesoporous silica shell is an interesting and novel approach for NIR-laser-triggered drug delivery applications, the preparation of these nanodevices can be challenging because of the reshaping or partial oxidation of the tips of AuNSts with a corresponding loss of their optical properties.<sup>36,42,43</sup> For this reason, a tight control of each synthetic step ([Figure 1](#)) is necessary to obtain

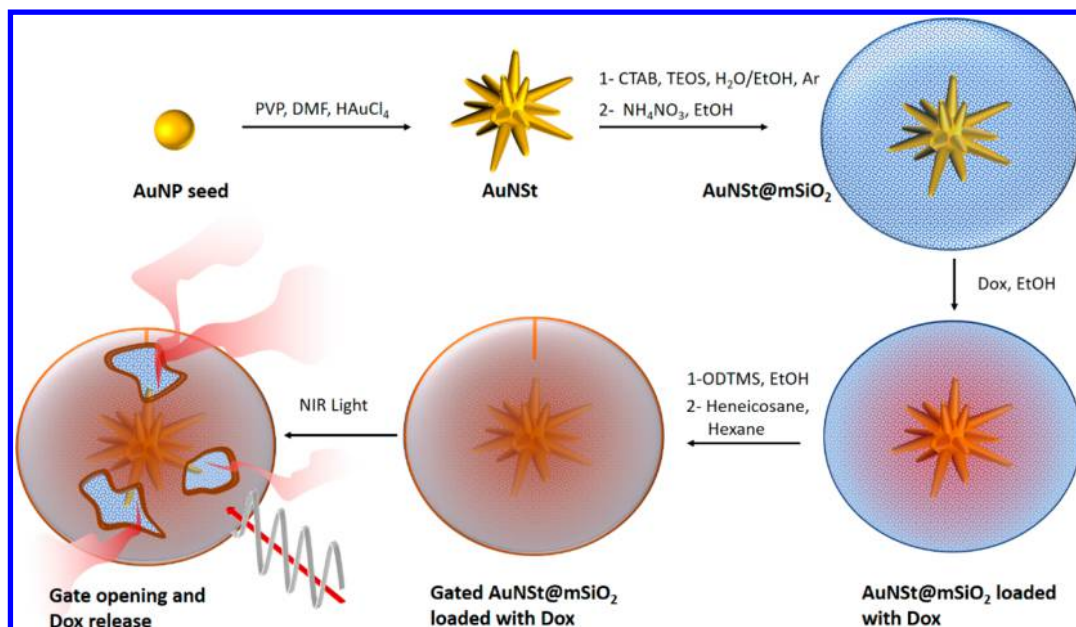


**Figure 1.** Representation of the drug photorelease system AuNSt@mSiO<sub>2</sub>@Dox@paraffin based on AuNSts coated with a mesoporous silica shell and paraffin as a thermosensitive molecular gate. The delivery of the entrapped cargo (Dox) is triggered by NIR laser irradiation.

nanoparticles with a homogeneous silica shell and mesopores, and suitable plasmonic properties. Several synthetic conditions including surfactant/TEOS ratio, temperature, inert atmosphere, etc. were tested to finally prepare AuNSt@mSiO<sub>2</sub> nanoparticles with minimum changes in the shape and absorption properties of the AuNSt core (*vide infra*).

AuNSts were obtained by the seeded growth method using polyvinylpyrrolidone (PVP) solution in *N,N*-dimethylformamide (DMF). This procedure is based on the chemical reduction of AuCl<sub>4</sub><sup>-</sup> complexes by DMF, and the subsequent deposition of gold atoms in the presence of PVP on the gold nanoparticles, acting as seeds. Nanoparticle size and morphology can be tuned varying the [HAuCl<sub>4</sub>]/[seed] molar ratio and the size of the seed.<sup>36</sup> Nanostars with sizes of 120 and 250 nm were synthesized using seeds (gold nanoparticles, AuNPs) of 15 and 40 nm, respectively (Figure S1). The average hydrodynamic diameters of these nanoparticles were consistent with TEM measurements (Figure 2a). The optical extinction spectra of an aqueous suspension of both sizes of AuNSts (Figure 2b) showed an absorption band/shoulder in the visible region, corresponding to LSPR of core electrons, and another band associated with LSPR of tip electrons,<sup>44</sup> whose position varied from 835 to 1050 nm when the AuNSt size increased.

In the first step of this research, characterization of the heating ability of uncoated AuNSts (120 nm) and PVP-coated AuNSts (250 nm) was carried out quantifying both single nanoparticle and bulk heating associated with electromagnetic irradiation. Using a temperature-sensitive lipid matrix, we directly assessed the plasmonic heating of single uncoated AuNSts and PVP-coated AuNSts, and the thermoplasmonic-associated temperature increase was measured. In the experiments, AuNSts were immobilized on a lipid bilayer with a well-known phase transition temperature incorporating fluorescent dyes with a preference for the liquid phase. The chamber was held at a temperature below the phase transition temperature, and by measuring the size of the melted area around the irradiated nanostructure (seen as the bright spots in the upper panels on Figure 2c–f), the temperature profile was quantified.

More details on this technique can be found in the following sections, and in refs 15–17. In the experiments, the particles were irradiated by a tightly focused NIR laser ( $\lambda = 1064$  nm). The phase-sensitive lipid fluorophore was FAST-DiO with a preference for the liquid state. During the experiment, the sample chamber was mounted on a temperature controller and kept at 28 °C, which is below the melting phase transition (33 °C).<sup>16</sup>

The steady-state temperature profile around an irradiated particle in an infinite medium is reasonably well-approximated as<sup>45</sup>

$$\Delta T(r) = \frac{CP}{r} \quad (1)$$

Here,  $C$  is a constant that includes the physical parameters describing the nanoparticle such as its absorption cross-section and the surrounding medium's thermal conductivity. Equation 1 is valid for  $r > R$ , where  $r$  is the distance to the particle's center and  $R$  the radius of the nanoparticle.  $P$  is the laser power.<sup>15</sup> At the rim of the melted area, the temperature is exactly the phase transition temperature, 33 °C. The distance to this rim from the center of the particle is denoted  $r_m$  and is proportional to  $P$ . Figure 2c shows  $r_m$  as a function of  $P$ , and the linear relation is evident. Fitting Equation S1 to the data shown in Figure 2c we obtain the temperature profile of the irradiated nanoparticle.

Figure 2d shows the temperature increase at the surface of the nanoparticle as a function of  $P$ . To find the temperature increase, we assumed that the average radius of the uncoated AuNSt was 60 nm (Figure 2a and Figure S1). The error bars show one standard deviation for measurements of 10 different AuNSts. The surface temperature of an uncoated AuNSt increased up to 400 °C at the applied laser powers without showing signs of deterioration of the particles.

On the basis of the experimental data we also inferred the absorption cross-section of gold nanostars using the following equation<sup>46</sup>

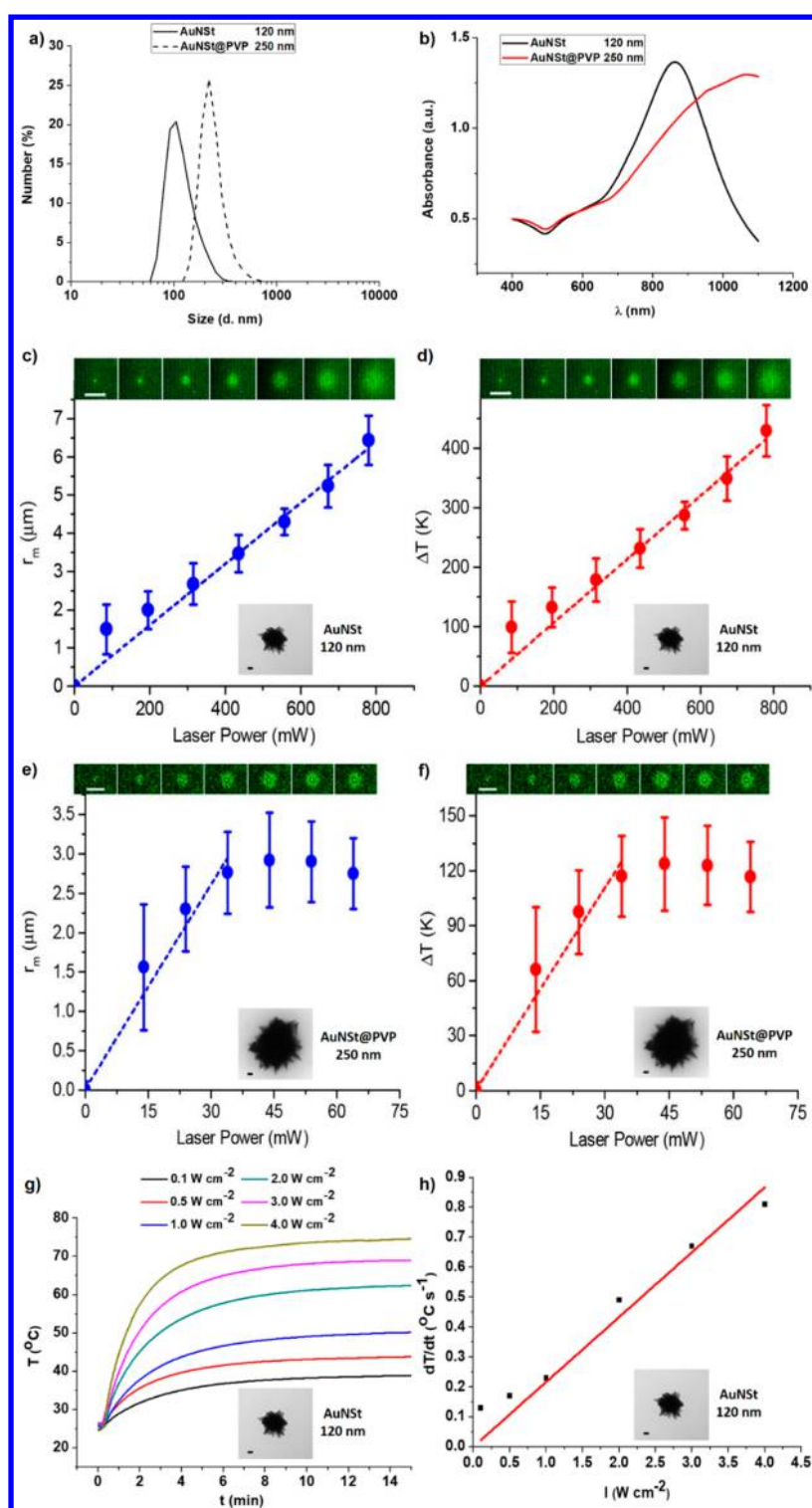


**Figure 2.** (a) Hydrodynamic diameter of uncoated and PVP-coated AuNSts by dynamic light scattering (DLS). (b) Optical extinction spectra of both AuNSts with different diameters. Quantification of the surface temperature of irradiated (c, d) uncoated and (e, f) PVP-coated AuNSts. (c, e) Symbols show the experimentally measured radius of the melted area around a laser-irradiated AuNSt as a function of laser power at the sample. (d, f) Experimentally extracted temperature increases on the surface of an irradiated AuNSt as a function of laser power. The upper panels show representative and corresponding confocal images of the melted area for laser power; the scale bar is  $10 \mu\text{m}$ . The error bars show one standard deviation, for measurements of  $n = 10$  different AuNSts, and the dashed lines show a linear fit to the data. NIR-laser-induced (808 nm) (g) bulk heating and (h) initial heating rate of uncoated AuNSt (120 nm) suspensions at different laser power densities. Insets: TEM images of (c, d, g, h) uncoated and (e, f) PVP-coated AuNSts. Scale bars:  $20 \text{ nm}$ .

$$C_{\text{abs}} = \frac{4\pi\bar{k}\Delta T_s R}{I} \quad (2)$$

where  $\Delta T_s$  is the increase of the nanoparticle's surface temperature,  $I$  is laser power density,  $R$  is the radius of the AuNSt, and  $\bar{k}$  is the heat conductivity of the combined glass

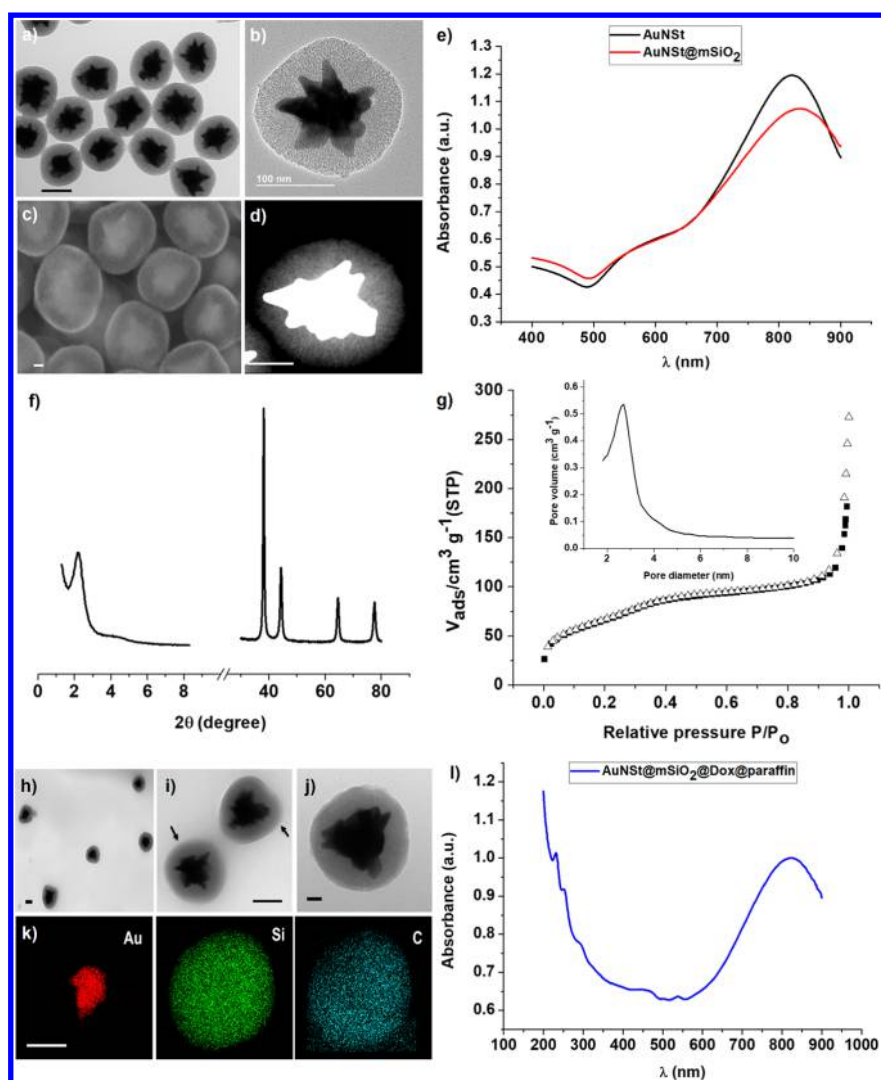


**Figure 3.** (a) TEM, (b) HR-TEM, (c) FE-SEM, and (d) DF-STEM images of AuNSt@mSiO<sub>2</sub> nanoparticles. Scale bars: (a) 100 nm, (d) 50 nm, (c) 20 nm. (e) Optical extinction spectra of AuNSt and AuNSt@mSiO<sub>2</sub> nanoparticles. (f) PXRD patterns and (g) N<sub>2</sub> adsorption–desorption isotherms of AuNSt@mSiO<sub>2</sub> nanoparticles (inset: pore size distribution). (h, i, j) TEM images of AuNSt@mSiO<sub>2</sub>@Dox@paraffin nanoparticles and (k) EDXS element mapping of Au, Si, and C. Scale bars: (h, i, k) 100 nm, (j) 20 nm. (l) Optical extinction spectrum of AuNSt@mSiO<sub>2</sub>@Dox@paraffin nanoparticles.

and water system at 300 K. Following ref 46, we approximate the latter as an average of  $k_{\text{glass}} = 1.1 \text{ W m}^{-1} \text{ K}^{-1}$  and  $k_{\text{water}} = 0.61 \text{ W m}^{-1} \text{ K}^{-1}$ .<sup>47</sup> Using eq 2, we calculated  $C_{\text{abs}} = 1012 \pm 145 \text{ nm}^2$  (assuming a laser focal spot diameter of  $1.95 \mu\text{m}$ ).

We also measured the temperature increase of an individual irradiated AuNSt with a PVP coating (Figure 2e,f). To find the temperature increase, we assumed that the average radius of a PVP-coated AuNSt was 125 nm (Figure 2a and Figure S1). Using eq 2, we find the absorption cross-section of PVP-coated AuNSts to be  $C_{\text{abs}} = 13763 \pm 2588 \text{ nm}^2$ , which is 14 times larger than that of uncoated AuNSts and 2.5 times larger than that of silica–gold nanoshells (shell thickness = 15 nm, core diameter = 120 nm).<sup>17</sup> These results agree well with previous work demonstrating large energy conversion efficiency of AuNSts.<sup>10–12</sup> Above a certain laser power ( $\sim 40 \text{ mW}$ ), however, the temperature does not increase with increasing laser power for the PVP-coated AuNSt. The surface temperature remains at  $\sim 120 \text{ }^\circ\text{C}$  + ambient temperature, hence at  $\sim 145 \text{ }^\circ\text{C}$ . This temperature is consistent with the melting temperature of PVP ( $150 \text{ }^\circ\text{C}$ ). Hence, the flattening of the

temperature curve probably indicates melting of the PVP coating. Hence, for a PVP-coated AuNSt the temperature increases steeply as a function of laser power, until the surface temperature reaches the melting temperature of the PVP coating. When melting is initiated, the plasmonic properties of the particle change tremendously. It is relatively normal that the plasmonic nanoparticles undergo structural changes following heating.<sup>48,49</sup> The plasmonic nanoparticle itself reaches a steady-state temperature within nanoseconds of irradiation. Moreover, the presence of a plateau (or maybe a slight decrease) in  $\Delta T$  as a function of laser power in Figure 2f indicates a continuous loss of plasmonic properties. Also, the temperature at which this happens is consistent with the known melting temperature of PVP.

These results show that, by a careful selection of the irradiating electromagnetic field power, it is possible to control the particle's temperature profile. For instance, at a laser power of 30 mW the surface temperature of a PVP-coated nanostar reaches  $120 \text{ }^\circ\text{C}$ , which should be high enough to produce cargo release from the AuNSt@mSiO<sub>2</sub> nanocarrier (*vide infra*).

To evaluate the heating capabilities of the bulk nanoparticles, we irradiated aqueous suspensions of uncoated AuNSts (120 nm) with a homemade NIR laser at 808 nm,<sup>40</sup> which match the LSPR band of the nanoparticles (Figure 2b) and measured the bulk temperature using a fiber-optic thermosensor. The temperature in nanoparticle suspensions ( $5.7 \times 10^9$  nanoparticles  $\text{mL}^{-1}$ ) upon 15 min of laser irradiation (808 nm) at different laser power densities,  $I$ , is shown in Figure 2g. The temperature rapidly increased and reached 70 °C at laser power density of 4  $\text{W cm}^{-2}$ . Both the initial bulk temperature increase rate (initial slope of  $T$  vs  $t$ ,  $\frac{dT}{dt}$ ) and the maximum temperature in the solution decreased when lower laser power densities were used. Also, the relation between  $\frac{dT}{dt}$  and  $I$  was linear (Figure 2h). The absorption cross-section of uncoated AuNSts can be inferred using the experimental data and eqs 3 and 4.<sup>9</sup>

$$\text{SAR} = C_s \rho_s \frac{dT}{dt} \quad (3)$$

$$\text{SAR} = \frac{NC_{\text{abs}}I}{V} \quad (4)$$

Here, SAR is the specific absorption rate per unit of volume, and  $C_s$  and  $\rho_s$  are the specific heat capacity and the density of the suspension, respectively.  $N$  is the number of nanoparticles, and  $V$  is the suspension volume. Using eqs 3 and 4, we calculated  $C_{\text{abs}} = 16\,000 \text{ nm}^2$ . For a comparison, in the experiments with single PVP-coated AuNSts returned a value of  $C_{\text{abs}} = 13\,763 \pm 2588 \text{ nm}^2$ , which is comparable to the bulk value of uncoated AuNSts. These values are larger than that reported for other plasmonic gold nanoparticles, demonstrating larger energy conversion efficiency of AuNSts upon laser irradiation at LSPR wavelengths.<sup>10–12</sup>

After the heating ability of AuNSts was analyzed, AuNSt@mSiO<sub>2</sub> nanoparticles were obtained by directly coating bare AuNSts (120 nm) with a MS shell. The preparation protocol is based on a surfactant-templated synthesis.<sup>43</sup> The formation of the MS shell over the AuNSts proceeds via four main steps that involve adsorption of cationic surfactant and formation of micelle assemblies on the nanoparticle's surface, hydrolysis of tetraethoxysilane (TEOS), a subsequent condensation reaction to form silica oligomers and deposition of silica oligomers on the micelle's surface, and controlled silica growth. The mesoporous coating is a critical process because AuNSts can be easily reshaped because of oxidation of tip gold atoms (for instance, in the presence of CTAB)<sup>50,51</sup> resulting in a decreased light absorption at 808 nm (laser wavelength), and a reduction of the light-to-heat conversion efficiency (Figures S2 and S3).

In the current study several synthetic parameters, such as temperature, reaction media, base used in the preparation of the MS shell, and CTAB/TEOS molar ratio, were identified as crucial to produce AuNSt@mSiO<sub>2</sub> nanoparticles with a suitable silica shell coating (in terms of pore organization and size) while minimizing reshaping of the gold core. In the final preparation of the AuNSt@mSiO<sub>2</sub> nanoparticles, (i) the shell coating processes were carried out at 25 °C, and (ii) the reaction medium was purged with argon to eliminate oxygen; (iii) a water/ethanol mixture was used as reaction medium to achieve a more controllable hydrolysis rate of the silica precursor (i.e., TEOS), and (iv) ammonia was used instead of other bases. (v) The CTAB/TEOS molar ratio was adjusted in

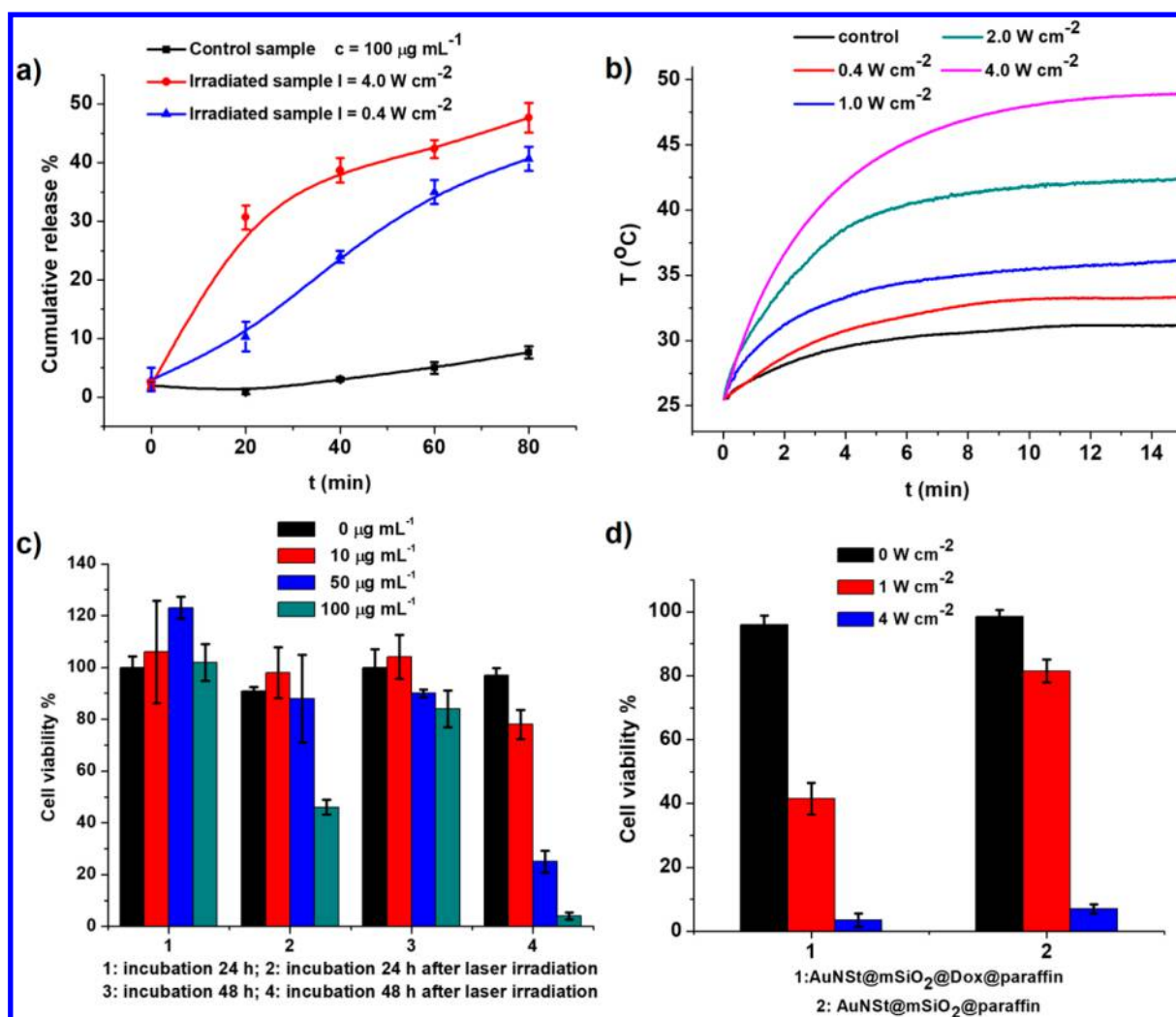
the 1.8–2.5 range, and the AuNSt concentration was set at ca.  $7\text{--}14 \times 10^{-12} \text{ M}$  ( $c(\text{Au}) = 1\text{--}2 \times 10^{-4} \text{ M}$ ).

Figure 3a–d and Figure S4 show the obtained AuNSt@mSiO<sub>2</sub> nanoparticles following this procedure with diameters that can vary between 150 and 200 nm. Fine adjustments of the thickness of the silica shell can be obtained by adjusting the amount of silica precursor in the reaction mixture. The optical extinction spectrum of aqueous suspension of the AuNSt@mSiO<sub>2</sub> nanoparticles showed that the NIR LSPR band slightly shifted to higher wavelengths as a result of the presence of the silica shell, which changes the surface refractive index (Figure 3e).<sup>18–23</sup>

Surfactant molecules from AuNSt@mSiO<sub>2</sub> were completely removed by an ion-exchange extraction process using ammonium nitrate solution in ethanol. The removal of CTAB from the nanoparticles was monitored by FT-IR spectroscopy and  $\zeta$  potential measurements (Figure S5). The characteristic peaks of CTAB at 2923, 2853 (C–H stretching), and 1478 (C–H bending)  $\text{cm}^{-1}$  were absent in the spectrum of the AuNSt@mSiO<sub>2</sub> nanoparticles after the extraction process. The change of the  $\zeta$  potential of nanoparticles from +32.5 to –45.3 mV also confirmed the removal of CTAB.

A detailed analysis of the nanoparticle's morphology was carried out using field-emission scanning electron microscopy (FE-SEM), high-resolution transmission electron microscopy (HR-TEM), and dark-field scanning transmission electron microscopy (DF-STEM). AuNSt@mSiO<sub>2</sub> nanoparticles contain a multibranching gold core and a MS shell with pores extending radially (Figure 3b–d and Figure S6). The geometry of the mesoporous channels of the silica shell is an important parameter which may determine the efficiency of drug loading and delivery behavior as it affects the diffusion of the drug within the mesoporous channels. Small-angle powder X-ray diffraction (PXRD) patterns of AuNSt@mSiO<sub>2</sub> nanoparticles exhibited a clear peak at  $2\theta = 2.20^\circ$ , which could be assigned to the (100) diffraction plane of a hexagonal unit cell.<sup>52</sup> This peak also suggested the presence of radial mesopore channels and an ordered mesostructure (Figure 3f). In the wide-angle PXRD pattern, four Au diffraction peaks were clearly discerned at  $2\theta = 38.16^\circ$ ,  $44.35^\circ$ ,  $64.60^\circ$ , and  $77.61^\circ$ , which can be indexed to (111), (200), (220), and (311) diffraction planes of the face-centered cubic gold lattice, respectively.<sup>53</sup> Moreover, N<sub>2</sub> adsorption–desorption isotherms of AuNSt@mSiO<sub>2</sub> nanoparticles indicated a Type IV curve for mesoporous materials. The average pore size was 2.6 nm, whereas the total pore volume and BET surface area were calculated to be  $0.25 \text{ cm}^3 \text{ g}^{-1}$  and  $241 \text{ m}^2 \text{ g}^{-1}$ , respectively (Figure 3g).<sup>21,22,24</sup>

AuNSt@mSiO<sub>2</sub> nanoparticles were loaded with the anti-cancer drug Dox, which can be easily detected using absorption (maximum absorption at  $\lambda = 480 \text{ nm}$ ) and fluorescence spectroscopy (maximum emission at  $\lambda = 555 \text{ nm}$ ;  $\lambda_{\text{exc}} = 488 \text{ nm}$ ). The external surface of Dox-loaded AuNSt@mSiO<sub>2</sub> was functionalized with a monolayer of octadecyltrimethoxysilane (ODTMS) and capped with a heneicosane coating. The hydrophobic ODTMS was used to facilitate the coating process of the thermosensitive paraffin layer. The paraffin coating formed a hydrophobic layer that blocked the pores and avoided leaks of the cargo (Figure 3h–k and Figures S7 and S8). Drug loading and external surface functionalization of AuNSt@mSiO<sub>2</sub> to obtain AuNSt@mSiO<sub>2</sub>@Dox@paraffin were also optimized to prepare a hybrid nanosystem with suitable plasmonic properties. The Dox concentration in the loading solution and the loading time were adjusted to be 500



**Figure 4.** (a) Cumulative release of Dox from AuNSt@mSiO<sub>2</sub>@Dox@paraffin aqueous suspensions and (b) NIR-light-induced heating of bulk nanoparticle suspensions at different laser power densities. (c) Viability of HeLa cells in the presence of AuNSt@mSiO<sub>2</sub>@Dox@paraffin nanoparticles (at different incubation times and concentrations) upon 808 nm laser irradiation at 4 W cm<sup>-2</sup> for 15 min. (d) Cell viability of HeLa cells in the presence of AuNSt@mSiO<sub>2</sub>@Dox@paraffin and AuNSt@mSiO<sub>2</sub>@paraffin nanoparticles upon laser irradiation (808 nm) at different laser power densities during 10 min.

$\mu\text{g mL}^{-1}$  and 12 h, respectively, to obtain nanoparticles with an LSPR band near 808 nm (Figure 3l).

The average hydrodynamic diameter of the nanoparticles increased from 228 to 300 nm after drug loading and paraffin coating processes, whereas the  $\zeta$  potential changed from  $-45.3$  to  $-17.0$  mV because of the presence of Dox in the mesoporous channels and the functionalization of silanol groups at the external surface of the nanoparticle with octadecyltrimethoxysilane (Figure S9). The overall fraction of organic material in the AuNSt@mSiO<sub>2</sub>@Dox@paraffin was estimated to be 25% by TGA measurement (Figure S10), while the loaded amount of Dox was 2.4% by spectrophotometric determination (Figure S11).

Although the nanocomposite surface was coated with a hydrophobic layer of paraffin, the surface charge remains high enough to form stable aqueous suspensions for bioapplications. The stability of the nanoparticle suspension was improved in DMEM for *in vitro* experiments with cells. The adsorption of different species (molecules and ions) onto the nanoparticle surface can avoid nanoparticle flocculation and enhance suspension stability in DMEM. The nanoparticles properly

interact with cells and can be internalized (*vide infra*). Moreover, the hybrid nanoparticles are stable in solid-state and aqueous suspensions at room temperature. However, when the nanoparticle suspension was heated at 60 °C during 48 h (for determination of Dox loading content), the silica shell was damaged, and the gold core was reshaped because of hydrolysis of silica and oxidation of gold, both processes favored at high temperatures. Furthermore, the LSPR band position shifted to lower wavelengths because of gold core reshaping (Figure S12).

Regarding the photothermal conversion efficiency of hybrid nanoparticles, eq 4 shows that the photothermal conversion efficiency is proportional to the used laser intensity and nanomaterial's absorption cross-section. Basically, at constant laser power (intensity), the photothermal conversion efficiency of different nanomaterials can be assessed comparing their absorption cross-sections. Comparing absorbance of AuNSt@mSiO<sub>2</sub> (Figure 3e) with the absorbance of AuNSt@mSiO<sub>2</sub>@Dox@paraffin (Figure 3l) at 808 nm reveals that their absorbance, and thereby their photothermal conversion efficiency, are nearly the same. Moreover, as the absorption

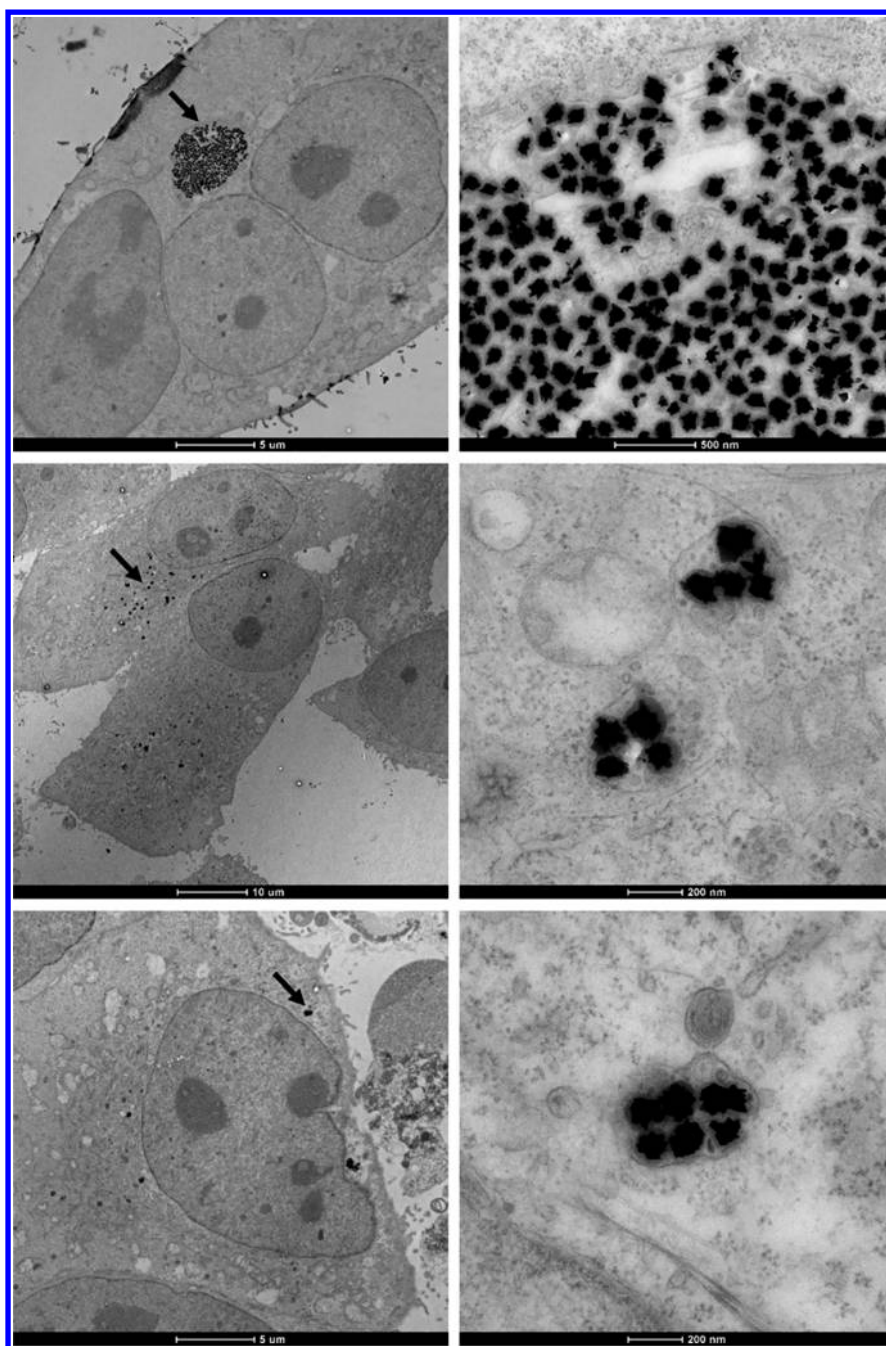


**Figure 5.** TEM pictures of HeLa cells after incubation with AuNSt@mSiO<sub>2</sub>@Dox@paraffin nanoparticles.

of Dox in water (Figure S11b) at 808 nm is very low, the cargo could be considered as transparent at this wavelength. This explains why there is essentially no difference in the photothermal conversion efficiency for nanomaterials with or without Dox at 808 nm.

Aqueous suspensions of AuNSt@mSiO<sub>2</sub>@Dox@paraffin nanoparticles were irradiated using a homemade NIR laser at 808 nm,<sup>40</sup> which matches the LSPR band of the nanoparticles (Figure 31). Cumulative release of Dox was determined using fluorescence spectroscopy. Irradiated AuNSt@mSiO<sub>2</sub>@Dox@paraffin samples showed a well-defined photodelivery profile. Around 30% of the total loaded drug was delivered in the first 20 min upon NIR light irradiation at power density of 4 W cm<sup>-2</sup>, whereas the nonirradiated control sample showed a negligible release, corroborating the gating efficacy of the

paraffin and the photothermal conversion efficiency of the gold nanostars (Figure 4a). Using these experimental conditions, a clear heating of the water within which the nanoparticles were suspended was observed (Figure 4b). The temperature of the bulk suspension under NIR irradiation was measured to be 49 °C while the temperature of the control sample (without NIR irradiation) was 30 °C. An enhancement of the temperature above the paraffin melting point ( $T_m = 39$  °C) provoked uncapping of the mesopores and dye release. These results are similar to those previously reported for drug photodelivery systems based on plasmonic Au nanoparticles with mesoporous gated silica shell, employing Au nanocages<sup>24</sup> and nanorods<sup>18–23</sup> as photothermal energy generators and polymers,<sup>19,24</sup> 1-tetradecanol,<sup>18</sup> DNA,<sup>20–22</sup> and supramolecular switches<sup>23</sup> as thermosensible gatekeepers.

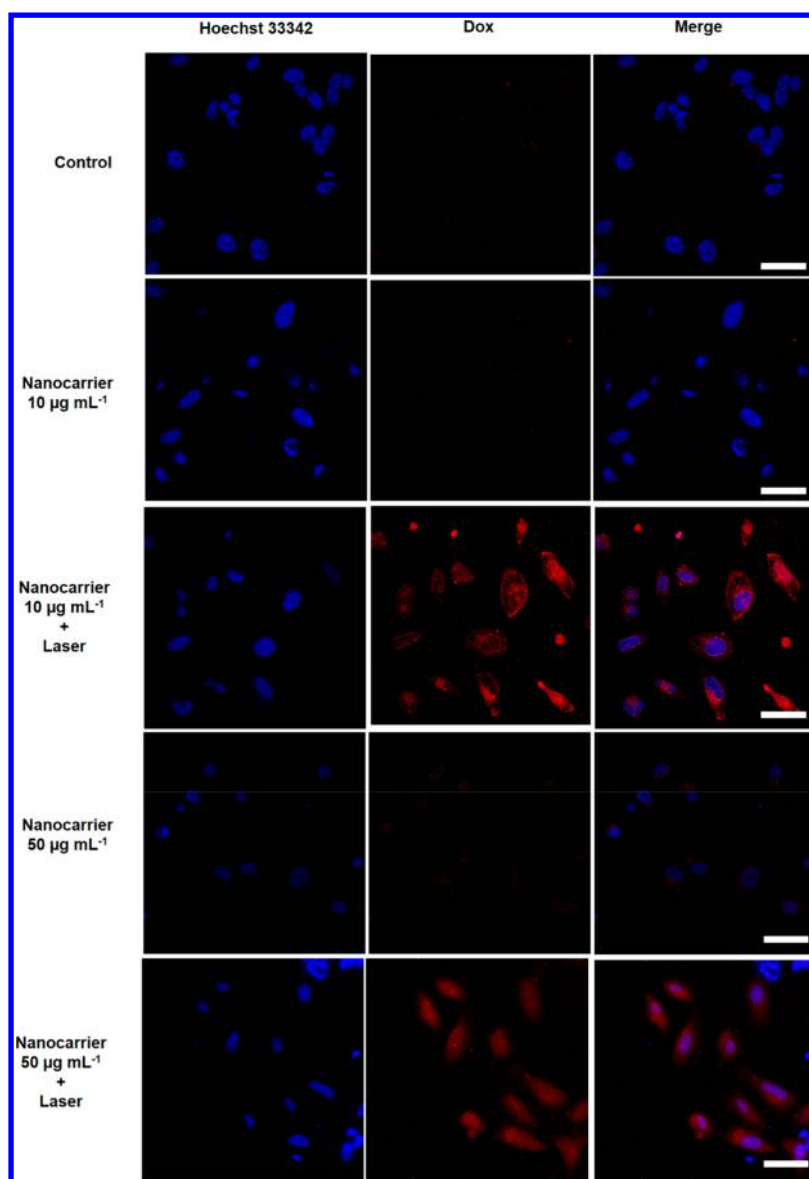


**Figure 6.** NIR-light-triggered release of Dox from AuNSt@mSiO<sub>2</sub>@Dox@paraffin nanoparticles in HeLa cells monitored by confocal laser scanning microscopy. From left to right: DNA marker (Hoechst 33342), Dox, and combined (merge) fluorescence channels. From top to bottom: control cells (control), nonirradiated cells after incubation with nanoparticles at 10  $\mu\text{g mL}^{-1}$  (nanocarrier 10  $\mu\text{g mL}^{-1}$ ), NIR-light-irradiated cells after incubation with nanoparticles at 10  $\mu\text{g mL}^{-1}$  (nanocarrier 10  $\mu\text{g mL}^{-1}$  + laser), nonirradiated cells after incubation with nanoparticles at 50  $\mu\text{g mL}^{-1}$  (nanocarrier 50  $\mu\text{g mL}^{-1}$ ), and NIR-light-irradiated cells after incubation with nanoparticles at 50  $\mu\text{g mL}^{-1}$  (nanocarrier 50  $\mu\text{g mL}^{-1}$  + laser). Scale bars: 50  $\mu\text{m}$ .

The NIR-induced heating profile and consequently the drug release can be modulated using different laser power densities (Figure 4a,b). For instance, the temperature increase ( $\Delta T$ ) of NIR-laser-irradiated suspensions of AuNSt@mSiO<sub>2</sub>@Dox@paraffin at 15 min was lower when irradiated by the lower laser power densities (24 °C at 4 W cm<sup>-2</sup>, 17 °C at 2 W cm<sup>-2</sup>, 11 °C at 1 W cm<sup>-2</sup>, and 8 °C at 0.4 W cm<sup>-2</sup>). In addition, the photothermal conversion efficiencies of hybrid nanoparticles are lower than that of AuNSts at the same mass concentration because of the fact that hybrid nanoparticles have a lower gold content. In Figures 4b and 2g we could see the NIR laser (808 nm) induced bulk heating of AuNSt@mSiO<sub>2</sub>@Dox@paraffin and AuNSt suspensions, respectively, both at 100  $\mu\text{g mL}^{-1}$ . Both the initial bulk temperature increase rate (initial slope of  $T$  vs  $t$ ,  $\frac{dT}{dt}$ ) and the maximum temperature in the solution at the

same laser power density were lower for hybrid nanoparticles. However, the photothermal conversion efficiency of hybrid nanoparticles was high enough for cancer therapy applications (hyperthermia and photothermal-triggered drug delivery) (*vide infra*).

Moreover, it is possible to induce Dox release even when an aqueous suspension of the AuNSt@mSiO<sub>2</sub>@Dox@paraffin nanoparticles was irradiated at a low laser power density that produced only a slight increase of the suspension temperature. The obtained result is consistent with a large temperature increase near the nanoparticle surface as a consequence of the high photothermal conversion efficiency of AuNSts that results in local paraffin melting and subsequent drug release. This observation agrees with the results found in the direct measurements of the local heating of AuNSt under laser irradiation (*vide ante*) in which it was found that the

temperature around the AuNSt easily increases over the melting point of paraffin, even at low laser powers. This supports the fact that Dox release from hybrid nanoparticles irradiated at low laser power density was observed, although the bulk temperature of the nanoparticle suspensions did not increase above the melting point of paraffin (Figures 2c,d and 4a,b).

NIR-light-triggered Dox delivery from AuNSt@mSiO<sub>2</sub>@Dox@paraffin nanoparticles in HeLa cells was performed to evaluate the potential application of nanoparticles in cancer therapy. The underlying idea is to design a system that could store drugs, with minimal leakage, and with the capability of releasing it upon irradiation. The therapeutic use of such a system is based on the quantity of Dox released upon irradiation. To find the critical concentration of AuNSt@mSiO<sub>2</sub>@Dox@paraffin that can exert some therapeutic effect over cells, in a first step we decided to use the irradiation conditions that ensured the maximum drug release (Figure 4c). Once the optimal AuNSt@mSiO<sub>2</sub>@Dox@paraffin concentration was set, we then decided to study the effect of laser power (Figure 4d). Moreover, the interaction of hybrid nanoparticles with cancer cells was tested monitoring the cell internalization of nanoparticles by TEM (Figure 5). Efficient nanoparticle uptake by cells was observed after incubation of cells with nanoparticle suspension in DMEM. Cells were incubated with nanoparticles at different concentrations, and then, they were irradiated at 4 W cm<sup>-2</sup> for 15 min and finally incubated during 24 or 48 h. Cell viability was assessed using a WST-1 assay after the incubation period (Figure 4c). In these experiments the irradiation at 4 W cm<sup>-2</sup> did not damage the cells. As could be seen in Figure 4c, the viability of cells without nanoparticles did not decrease after laser irradiation and incubation during 24 and 48 h (black bars in groups 2 and 4). In fact, there are some reports in which higher laser power densities were used for *in vitro* and *in vivo* photothermal therapy experiments.<sup>8</sup> Moreover, nonirradiated nanoparticles showed almost no cytotoxicity toward HeLa cells, thus demonstrating that Dox was efficiently encapsulated inside the mesoporous shell because of the paraffin shell that prohibits leaking of the drug, even at high nanocarrier concentrations and incubation times. However, cell viability decreased when the nanoparticles were irradiated with a 808 nm laser. This effect was most remarkable at larger nanoparticle concentrations and incubation times. NIR light provoked an increase of nanoparticle's surface temperature leading to paraffin melting and Dox delivery. Larger amounts of Dox were released at higher nanocarrier concentrations and incubation times, producing consequently an enhanced cell-killing effect.

For an evaluation of the independent effects of hyperthermia and Dox release, cells were incubated with AuNSt@mSiO<sub>2</sub>@Dox@paraffin nanoparticles or with similar nanoparticles without payload (AuNSt@mSiO<sub>2</sub>@paraffin). Cells were irradiated at different laser power densities and then incubated for 48 h. A significant difference of the cell-killing efficacy for these two types of nanoparticles upon NIR irradiation at 1 W cm<sup>-2</sup> was made evident (Figure 4d). The viability of cells treated with AuNSt@mSiO<sub>2</sub>@paraffin (without payload) decreased to 80% upon NIR irradiation at 1 W cm<sup>-2</sup>. NIR-light-induced heating of bulk AuNSt@mSiO<sub>2</sub>@Dox@paraffin nanoparticle suspensions at different laser power densities is shown in Figure 4b. The temperature in nanoparticle suspensions (100 μg mL<sup>-1</sup>) reached 36 °C [the temperature increase ( $\Delta T$ ) was 11 °C] upon 15 min of 808 nm laser

irradiation at 1 W cm<sup>-2</sup>. Although the temperature of the nanoparticle suspension did not increase above 42 °C upon irradiation, the temperature at the nanoparticle surface can reach higher values inside the cells provoking the reduction of cell viability. Then, the decrease of cell viability (20%) is attributed to the effect of hyperthermia alone. In addition, a more pronounced decrease of the cell viability was obtained when cells were treated with Dox-loaded nanoparticles upon NIR irradiation at 1 W cm<sup>-2</sup>. This effect could be attributed to the activation of Dox released from nanoparticles, since there is essentially no difference in the photothermal conversion efficiency for nanomaterials with or without Dox at 808 nm, thus allowing for a synergistic combination of hyperthermia and chemotherapy.

Furthermore, NIR-light-triggered delivery of Dox from hybrid nanocarriers in HeLa cells was tested by confocal laser scanning microscopy (Figure 6). Cells were stained with the DNA-marker dye Hoechst 33342, and the intracellular delivery of Dox after laser irradiation was monitored by measuring the fluorescence signals of both dyes. Whereas a negligible Dox fluorescence signal can be observed in nonirradiated samples, an increase of Dox fluorescence in cells after laser irradiation was made evident, corroborating the intracellular cargo release from the nanocarrier activated by NIR light irradiation. These results show that paraffin-capped AuNSt@mSiO<sub>2</sub> nanoparticles are an outstanding platform for NIR-light-triggered drug delivery in cancer therapy applications. Moreover, the method presented allows for obtaining nanoparticles with a good quality of the silica shell while maintaining adequate and stable plasmonic properties of AuNSts for NIR-triggered drug photorelease applications.

## CONCLUSIONS

In summary, we have described a novel drug photorelease system based on AuNSts coated with a MS shell and capped with paraffin as a suitable thermosensitive molecular gate. The heating ability of AuNSts upon electromagnetic irradiation was quantified by irradiating a single AuNSt on a temperature-sensitive biological matrix. The surface temperature of uncoated AuNSts could easily reach hundreds of degrees (°C), even at relatively low laser powers. Using larger PVP-coated AuNSts caused the temperature to increase even more quickly with laser power, probably because the increase of nanoparticle size induced a red shift, thus displacing the LSPR peak further toward the irradiating laser wavelength. AuNSts were coated with a MS shell using a surfactant-templated synthesis at 25 °C. Several synthetic conditions including surfactant/TEOS ratio, temperature, inert atmosphere, etc. were tested to finally prepare AuNSt@mSiO<sub>2</sub> nanoparticles with minimum changes in the shape and absorption properties of the AuNSt core. AuNSt@mSiO<sub>2</sub> was loaded with Dox and capped with paraffin heneicosane. AuNSt@mSiO<sub>2</sub>@Dox@paraffin nanoparticles showed no leak of cargo in aqueous solutions, whereas a significant payload delivery was observed upon NIR irradiation even at 0.4 W cm<sup>-2</sup>. Dox-loaded nanoparticles showed no cytotoxicity toward HeLa cells, until they were irradiated with 808 nm laser, provoking paraffin melting and drug release. We believe that the method here reported for the preparation of the AuNSt@mSiO<sub>2</sub>@paraffin system can be of general use for the fabrication of new drug photodelivery systems containing AuNSts, with minimal leaks and low laser power requirements, two characteristics

highly required for their implementation in enhanced chemotherapy.

## ■ ASSOCIATED CONTENT

### 📄 Supporting Information

The Supporting Information is available free of charge on the ACS Publications website at DOI: [10.1021/acsami.8b08395](https://doi.org/10.1021/acsami.8b08395).

Additional TEM images, extinction spectra, FT-IR spectra, EDXS, DLS, and TG analysis (PDF)

## ■ AUTHOR INFORMATION

### Corresponding Authors

\*E-mail: [oddershede@nbi.ku.dk](mailto:oddershede@nbi.ku.dk).

\*E-mail: [rmaez@quim.upv.es](mailto:rmaez@quim.upv.es).

### ORCID

Akbar Samadi: [0000-0002-5754-2164](https://orcid.org/0000-0002-5754-2164)

Roberto Cao-Milán: [0000-0002-5935-2313](https://orcid.org/0000-0002-5935-2313)

Elena Aznar: [0000-0003-0361-3876](https://orcid.org/0000-0003-0361-3876)

Ramón Martínez-Mañez: [0000-0001-5873-9674](https://orcid.org/0000-0001-5873-9674)

### Notes

The authors declare no competing financial interest.

## ■ ACKNOWLEDGMENTS

The authors gratefully acknowledge financial support from the Spanish Government (Projects AGL2015-70235-C2-2-R and MAT2015-64139-C4-1-R), the Generalitat Valenciana (Project PROMETEOII/2014/047), and European Union (Programme European Union—Action 2—Erasmus Mundus Partnerships, Grant—2014-0870/001-001). A. Samadi and L. B. Oddershede acknowledge financial support from the Novo Nordisk Foundation (NNF14OC0011361) and from the Danish National Research Foundation (DNRF116). A. H. Montoto thanks Erasmus Mundus Programme for his PhD scholarship at EuroInkaNet project. The authors thank UPV electron microscopy and CIPF confocal and electron microscopy services for technical support.

## ■ REFERENCES

- (1) Aznar, E.; Oroval, M.; Pascual, L.; Murguía, J. R.; Martínez-Mañez, R.; Sancenón, F. Gated Materials for on-Command Release of Guest Molecules. *Chem. Rev.* **2016**, *116*, 561–718.
- (2) Wang, D.; Liu, B.; Quan, Z.; Li, C.; Hou, Z.; Xing, B.; Lin, J. New Advances on the Marrying of UCNPs and Photothermal Agents for Imaging-Guided Diagnosis and the Therapy of Tumors. *J. Mater. Chem. B* **2017**, *5*, 2209–2230.
- (3) Liu, B.; Li, C.; Cheng, Z.; Hou, Z.; Huang, S.; Lin, J. Functional Nanomaterials for Near-Infrared Triggered Cancer Therapy. *Biomater. Sci.* **2016**, *4*, 890–909.
- (4) Fan, W.; Yung, B.; Huang, P.; Chen, X. Nanotechnology for Multimodal Synergistic Cancer Therapy. *Chem. Rev.* **2017**, *117*, 13566–13638.
- (5) Zhang, L.; Chen, Y.; Li, Z.; Li, L.; Saint-Cricq, P.; Li, C.; Lin, J.; Wang, C.; Su, Z.; Zink, J. I. Tailored Synthesis of Octopus-Type Janus Nanoparticles for Synergistic Actively-Targeted and Chemo-Photothermal Therapy. *Angew. Chem., Int. Ed.* **2016**, *55*, 2118–2121.
- (6) Zhang, L.; Wang, T.; Yang, L.; Liu, C.; Wang, C.; Liu, H.; Wang, Y. A.; Su, Z. General Route to Multifunctional Uniform Yolk/Mesoporous Silica Shell Nanocapsules: A Platform for Simultaneous Cancer-Targeted Imaging and Magnetically Guided Drug Delivery. *Chem. - Eur. J.* **2012**, *18*, 12512–12521.
- (7) Lim, W. Q.; Gao, Z. Plasmonic Nanoparticles in Biomedicine. *Nano Today* **2016**, *11*, 168–188.
- (8) Abadeer, N. S.; Murphy, C. J. Recent Progress in Cancer Thermal Therapy Using Gold Nanoparticles. *J. Phys. Chem. C* **2016**, *120*, 4691–4716.
- (9) Pino, P. d.; Pelaz, B. Hyperthermia Using Inorganic Nanoparticles. In *Frontiers of Nanoscience*; Fuente, J. M. d. I., Grazu, V., Eds.; Elsevier Ltd: Oxford, 2012; pp 309–335.
- (10) Jaque, D.; Maestro, L. M.; Rosal, B. d.; Haro-Gonzalez, P.; Benayas, A.; Plaza, J. L.; Rodríguez, E. M.; Solé, J. G. Nanoparticles for Photothermal Therapies. *Nanoscale* **2014**, *6*, 9494–9530.
- (11) Maestro, L. M.; Haro-González, P.; Sánchez-Iglesias, A.; Liz-Marzán, L. M.; Solé, J. G.; Jaque, D. Quantum Dot Thermometry Evaluation of Geometry Dependent Heating Efficiency in Gold Nanoparticles. *Langmuir* **2014**, *30*, 1650–1658.
- (12) Wang, Y.; Black, K. C. L.; Luehmann, H.; Li, W.; Zhang, Y.; Cai, X.; Wan, D.; Liu, S.-Y.; Li, M.; Kim, P.; Li, Z.-Y.; Wang, L. V.; Liu, Y.; Xia, Y. Comparison Study of Gold Nanohexapods, Nanorods, and Nanocages for Photothermal Cancer Treatment. *ACS Nano* **2013**, *7*, 2068–2077.
- (13) Trigari, S.; Rindi, A.; Margheri, G.; Sottini, S.; Dellepiane, G.; Giorgetti, E. Synthesis and Modelling of Gold Nanostars with Tunable Morphology and Extinction Spectrum. *J. Mater. Chem.* **2011**, *21*, 6531–6540.
- (14) Rodríguez-Oliveros, R.; Sánchez-Gil, J. A. Gold Nanostars as Thermoplasmonic Nanoparticles for Optical Heating. *Opt. Express* **2012**, *20*, 621–626.
- (15) Bendix, P. M.; Reihani, S. N. S.; Oddershede, L. B. Direct Measurements of Heating by Electromagnetically Trapped Gold Nanoparticles on Supported Lipid Bilayers. *ACS Nano* **2010**, *4*, 2256–2262.
- (16) Ma, H.; Tian, P.; Pello, J.; Bendix, P. M.; Oddershede, L. B. Heat Generation by Irradiated Complex Composite Nanostructures. *Nano Lett.* **2014**, *14*, 612–619.
- (17) Jørgensen, J. T.; Norregaard, K.; Tian, P.; Bendix, P. M.; Kjaer, A.; Oddershede, L. B. Single Particle and PET-Based Platform for Identifying Optimal Plasmonic Nano-Heaters for Photothermal Cancer Therapy. *Sci. Rep.* **2016**, *6*, 30076–30086.
- (18) Liu, J.; Detrembleur, C.; Pauw-Gillet, M.-C. D.; Mornet, S.; Jérôme, C.; Duguet, E. Gold Nanorods Coated with Mesoporous Silica Shell as Drug Delivery System for Remote near Infrared Light-Activated Release and Potential Phototherapy. *Small* **2015**, *11*, 2323–2332.
- (19) Tang, H.; Shen, S.; Guo, J.; Chang, B.; Jiang, X.; Yang, W. Gold Nanorods@mSiO<sub>2</sub> with a Smart Polymer Shell Responsive to Heat/Near-Infrared Light for Chemo-Photothermal Therapy. *J. Mater. Chem.* **2012**, *22*, 16095–16103.
- (20) Chang, Y.-T.; Liao, P.-Y.; Sheu, H.-S.; Tseng, Y.-J.; Cheng, F.-Y.; Yeh, C.-S. Near-Infrared Light-Responsive Intracellular Drug and Sirna Release Using Au Nanoensembles with Oligonucleotide-Capped Silica Shell. *Adv. Mater.* **2012**, *24*, 3309–3314.
- (21) Yang, X.; Liu, X.; Liu, Z.; Pu, F.; Ren, J.; Qu, X. Near-Infrared Light-Triggered, Targeted Drug Delivery to Cancer Cells by Aptamer Gated Nanovehicles. *Adv. Mater.* **2012**, *24*, 2890–2895.
- (22) Li, N.; Yu, Z.; Pan, W.; Han, Y.; Zhang, T.; Tang, B. A Near-Infrared Light-Triggered Nanocarrier with Reversible DNA Valves for Intracellular Controlled Release. *Adv. Funct. Mater.* **2013**, *23*, 2255–2262.
- (23) Li, H.; Tan, L.-L.; Jia, P.; Li, Q.-L.; Sun, Y.-L.; Zhang, J.; Ning, Y.-Q.; Yu, J.; Yang, Y.-W. Near-Infrared Light-Responsive Supramolecular Nanovalve Based on Mesoporous Silica-Coated Gold Nanorods. *Chem. Sci.* **2014**, *5*, 2804–2808.
- (24) Yang, J.; Shen, D.; Zhou, L.; Li, W.; Li, X.; Yao, C.; Wang, R.; El-Toni, A. M.; Zhang, F.; Zhao, D. Spatially Confined Fabrication of Core-Shell Gold Nanocages@Mesoporous Silica for Near-Infrared Controlled Photothermal Drug Release. *Chem. Mater.* **2013**, *25*, 3030–3037.
- (25) Liu, Y.; Yuan, H.; Kersey, F. R.; Register, J. K.; Parrott, M. C.; Vo-Dinh, T. Plasmonic Gold Nanostars for Multi-Modality Sensing and Diagnostics. *Sensors* **2015**, *15*, 3706–3720.

- (26) Yuan, H.; Gomez, J. A.; Chien, J. S.; Zhang, L.; Wilson, C. M.; Li, S.; Fales, A. M.; Liu, Y.; Grant, G. A.; Mirotsov, M.; Dzau, V. J.; Vo-Dinh, T. Tracking Mesenchymal Stromal Cells Using an Ultra-Bright Tat-Functionalized Plasmonic-Active Nanoplatfrom. *J. Biophotonics* **2016**, *9*, 406–413.
- (27) Liu, Y.; Yuan, H.; Fales, A. M.; Register, J. K.; Vo-Dinh, T. Multifunctional Gold Nanostars for Molecular Imaging and Cancer Therapy. *Front. Chem.* **2015**, *3*, 1–7.
- (28) Espinosa, A.; Silva, A. K. A.; Sánchez-Iglesias, A.; Grzelczak, M.; Péchoux, C.; Desboeufs, K.; Liz-Marzán, L. M.; Wilhelm, C. Cancer Cell Internalization of Gold Nanostars Impacts Their Photothermal Efficiency in Vitro and in Vivo: Toward a Plasmonic Thermal Fingerprint in Tumoral Environment. *Adv. Healthcare Mater.* **2016**, *5*, 1040–1048.
- (29) Turkevich, J.; Stevenson, P. C.; Hillier, J. A Study of the Nucleation and Growth Processes in the Synthesis of Colloidal Gold. *Discuss. Faraday Soc.* **1951**, *11*, 55–75.
- (30) Enustun, B. V.; Turkevich, J. Coagulation of Colloidal Gold. *J. Am. Chem. Soc.* **1963**, *85*, 3317–3328.
- (31) Frens, G. Controlled Nucleation for the Regulation of the Particle Size in Monodisperse Gold Suspensions. *Nature, Phys. Sci.* **1973**, *241*, 20–22.
- (32) Bastús, N. G.; Comenge, J.; Puentes, V. Kinetically Controlled Seeded Growth Synthesis of Citrate-Stabilized Gold Nanoparticles of up to 200 nm: Size Focusing Versus Ostwald Ripening. *Langmuir* **2011**, *27*, 11098–11105.
- (33) Graf, C.; Vossen, D. L. J.; Imhof, A.; Blaaderen, A. v A General Method to Coat Colloidal Particles with Silica. *Langmuir* **2003**, *19*, 6693–6700.
- (34) Scarabelli, L.; Grzelczak, M.; Liz-Marzán, L. M. Tuning Gold Nanorod Synthesis through Pre-Reduction with Salicylic Acid. *Chem. Mater.* **2013**, *25*, 4232–4238.
- (35) Hendel, T.; Wuithschick, M.; Kettemann, F.; Birnbaum, A.; Rademann, K.; Polte, J. r. In Situ Determination of Colloidal Gold Concentrations with Uv–Vis Spectroscopy: Limitations and Perspectives. *Anal. Chem.* **2014**, *86*, 11115–11124.
- (36) Barbosa, S.; Agrawal, A.; Rodríguez-Lorenzo, L.; Pastoriza-Santos, I.; Alvarez-Puebla, R. A.; Kornowski, A.; Weller, H.; Liz-Marzán, L. M. Tuning Size and Sensing Properties in Colloidal Gold Nanostars. *Langmuir* **2010**, *26*, 14943–14950.
- (37) Senthil Kumar, P.; Pastoriza-Santos, I.; Rodríguez-González, B.; Abajo, F. J. G. d.; Liz-Marzán, L. M. High-Yield Synthesis and Optical Response of Gold Nanostars. *Nanotechnology* **2008**, *19*, 015606–015612.
- (38) Khoury, C. G.; Vo-Dinh, T. Gold Nanostars for Surface-Enhanced Raman Scattering: Synthesis, Characterization and Optimization. *J. Phys. Chem. C* **2008**, *112*, 18849–18859.
- (39) Aznar, E.; Mondragón, L.; Ros-Lis, J. V.; Sancenón, F.; Marcos, M. D.; Martínez-Mañez, R.; Soto, J.; Pérez-Payá, E.; Amorós, P. Finely Tuned Temperature-Controlled Cargo Release Using Paraffin-Capped Mesoporous Silica Nanoparticles. *Angew. Chem.* **2011**, *123*, 11368–11371.
- (40) Montes-Robles, R.; Hernández, A.; Ibáñez, J.; Masot-Peris, R.; Torre, C. d. l.; Martínez-Mañez, R.; García-Breijo, E.; Fraile, R. Design of a Low-Cost Equipment for Optical Hyperthermia. *Sens. Actuators, A* **2017**, *255*, 61–70.
- (41) Richardson, A. C.; Reihani, N.; Oddershede, L. B. Combining Confocal Microscopy with Precise Force-Scope Optical Tweezers. *Proc. SPIE* **2006**, *6326*, 632628–632638.
- (42) Kedia, A.; Kumar, P. S. Controlled Reshaping and Plasmon Tuning Mechanism of Gold Nanostars. *J. Mater. Chem. C* **2013**, *1*, 4540–4549.
- (43) Sanz-Ortiz, M. N.; Sentosun, K.; Bals, S.; Liz-Marzán, L. M. Templated Growth of Surface Enhanced Raman Scattering-Active Branched Gold Nanoparticles within Radial Mesoporous Silica Shells. *ACS Nano* **2015**, *9*, 10489–10497.
- (44) Guerrero-Martínez, A.; Barbosa, S.; Pastoriza-Santos, I.; Liz-Marzán, L. M. Nanostars Shine Bright for You: Colloidal Synthesis, Properties and Applications of Branched Metallic Nanoparticles. *Curr. Opin. Colloid Interface Sci.* **2011**, *16*, 118–127.
- (45) Goldenberg, H.; Tranier, C. J. Heat Flow in an Infinite Medium Heated by a Sphere. *Br. J. Appl. Phys.* **1952**, *3*, 296–298.
- (46) Baffou, G.; Berto, P.; Ureña, E. B.; Quidant, R.; Monneret, S.; Polleux, J.; Rigneault, H. Photoinduced Heating of Nanoparticle Arrays. *ACS Nano* **2013**, *7*, 6478–6488.
- (47) Powell, R. W.; Ho, C. Y.; Liley, P. E. Thermal Conductivity of Selected Materials. *National Standard Reference Data Series- National Bureau of Standards* **1966**, 1–165.
- (48) Ma, H.; Bendix, P. M.; Oddershede, L. B. Large-Scale Orientation Dependent Heating from a Single Irradiated Gold Nanorod. *Nano Lett.* **2012**, *12*, 3954–3960.
- (49) Samadi, A.; Klingberg, H.; Jauffred, L.; Kjær, A.; Bendix, P. M.; Oddershede, L. B. Platinum Nanoparticles: A Non-Toxic, Effective and Thermally Stable Alternative Plasmonic Material for Cancer Therapy and Bioengineering. *Nanoscale* **2018**, *10*, 9097–9107.
- (50) Rodríguez-Fernández, J.; Pérez-Juste, J.; Mulvaney, P.; Liz-Marzán, L. M. Spatially-Directed Oxidation of Gold Nanoparticles by Au(III)-CTAB Complexes. *J. Phys. Chem. B* **2005**, *109*, 14257–14261.
- (51) Zheng, Y.; Zeng, J.; Ruditskiy, A.; Liu, M.; Xia, Y. Oxidative Etching and Its Role in Manipulating the Nucleation and Growth of Noble-Metal Nanocrystals. *Chem. Mater.* **2014**, *26*, 22–33.
- (52) Nooney, R. I.; Thirunavukkarasu, D.; Chen, Y.; Josephs, R.; Ostafin, A. E. Self-Assembly of Mesoporous Nanoscale Silica/Gold Composites. *Langmuir* **2003**, *19*, 7628–7637.
- (53) Liu, W.; Zhu, Z.; Deng, K.; Li, Z.; Zhou, Y.; Qiu, H.; Gao, Y.; Che, S.; Tang, Z. Gold Nanorod@Chiral Mesoporous Silica Core-Shell Nanoparticles with Unique Optical Properties. *J. Am. Chem. Soc.* **2013**, *135*, 9659–9664.